RESEARCH ARTICLE

Large-Eddy Simulation of the Effects of Wind-Direction Fluctuations on Turbulent Flow and Gas Dispersion Within a Cubical Canopy

Takenobu Michioka[1] · Hiroshi Takimoto[2] · Hiroki Ono[2] · Ayumu Sato[2]

Abstract

Large-eddy simulation of turbulent flow and gas dispersion in a cubical canopy is used to investigate the effect of wind-direction fluctuations on gas dispersion. Square blocks are set at regular intervals on the bottom surface, with line sources placed within the first, second, third, fifth and seventh rows. Large-eddy simulation without wind-direction fluctuations produces a good prediction of the mean streamwise velocity component, and the standard deviations of the fluctuations in the streamwise and spanwise velocity components, obtained from a wind-tunnel experiment. Wind-direction fluctuations marginally affect the mean streamwise velocity component above the canopy in the first row, and do not significantly affect the component beyond the third row. The standard deviations of the fluctuations in the streamwise and spanwise velocity components above the canopy are also affected by wind-direction fluctuations, but within the canopy the components are less sensitive to the fluctuations beyond the third row. The spatially-averaged concentrations within the canyon with wind-direction fluctuations before the third row are marginally greater than concentrations without the fluctuations, but they are essentially identical beyond the fifth row. The low-frequency turbulent flow that passes through the canyon is generated with and without wind-direction fluctuations.

Keywords Gas dispersion · Large-eddy simulation · Low-frequency turbulent flow · Urban canopy · Wind-direction fluctuation

1 Introduction

With the increasing availability of powerful supercomputers, high resolution numerical models (e.g., large-eddy simulation, LES) have become an increasingly attractive tool for

✉ Takenobu Michioka
michioka@mech.kindai.ac.jp

[1] Faculty of Science and Engineering, Kindai University, 3-4-1 Kowakae, Higashiōsaka, Osaka 577-8502, Japan

[2] Environmental Science Research Laboratory, Central Research Institute of Electric Power Industry, 1646 Abiko, Abiko-shi, Chiba-ken 270-1194, Japan

simulating pollutant dispersion in an urban canopy. Previous numerical models focused primarily on pollutant dispersion in an urban canopy under steady turbulent flow (e.g. Cai et al. 2008; Cheng and Liu 2011). Tominaga and Stathopoulos (2011) implemented Reynolds-averaged Navier–Stokes (RANS) modelling and large-eddy simulation (LES) for pollutant dispersion from a point source within a three-dimensional (3D) street canyon. A comparison of the mean concentrations for the RANS and LES models from wind-tunnel experimental data indicated that the LES model provided better results of the mean concentration distribution than the RANS model. Michioka et al. (2011, 2014) implemented LES for pollutant dispersal from a line source at the bottom surface of a street canyon for idealized two-dimensional (2D) and 3D street canyons. They applied a periodic boundary condition for the velocity in the streamwise and spanwise directions, and fully-developed turbulent flow was generated above the street canyon. The mean concentration obtained by LES was in good agreement with that obtained from wind-tunnel experiments (Meroney et al. 1996; Pavageau and Schatzmann 1999). Branford et al. (2011) implemented direct numerical simulation for a passive scalar in a regular array of cubical obstacles and concluded that 32^3 grid points per blocks were sufficient for simulating gas dispersion in an idealized urban canyon. For a complex urban canopy, Xie and Castro (2009) and Xie (2011) implemented LES to investigate flow and dispersion within an urban area at a DAPPLE (Dispersion of air pollution and its penetration into the local environment) project site in Central London (Arnold et al. 2004), and demonstrated that LES can reproduce the mean and root-mean-square concentrations obtained in wind-tunnel experiments. Nozu and Tamura (2012) used a LES model for gas dispersion emitted from a point source on the ground in Tokyo, Japan, and reported that the mean concentration was in good agreement with that obtained by wind-tunnel experiments. Michioka et al. (2013) implemented LES for an actual urban area under steady inlet boundary conditions, and reported that the vertical distributions of the mean concentration were similar to those obtained in the wind-tunnel experiments. Therefore, LES can reproduce gas dispersion in an urban area under steady turbulent flow when the grid resolution and computational scheme are accurately selected.

The above studies estimated the mean concentrations averaged over 3–10 min, but 1-h averaged concentrations are commonly used for ambient air-quality regulations adopted in numerous countries. A typical LES under steady turbulent flow might not estimate 1-h averaged concentrations, as meteorological influences such as fluctuations in the wind direction cannot be considered. Therefore, the effect of meteorological influences on gas dispersion in an urban area needs to be investigated for the accurate prediction of 1-h averaged concentrations.

An et al. (2013) investigated the effect of the inflow turbulence intensity on wind and turbulence profiles within both regular and irregular building arrays using a RANS model with a realizable k-ε turbulence model. They reported that the wind speed was not significantly affected by the turbulent-kinetic-energy profiles of the turbulent inflow and the turbulence within the canopy was dominated by the upstream building array. Murena and Mele (2014) implemented a 2D unsteady RANS model to investigate the effect of short-term wind-speed variations on pollutant removal from a 2D street canyon with a height-to-width ratio of three. Short-term variations in wind speed were simulated assuming a sinusoidal function at frequencies from 0.025 to 1 Hz, which were rapid unidirectional perturbations as opposed to mesoscale disturbances. The results indicated that pollutant removal is enhanced as the frequency decreases. Duan and Ngan (2018) investigated the effect of low frequency perturbations on turbulent flow within a street canyon using LES, and reported that the flow pattern and turbulence were not significantly sensitive to the time-dependent forcing. The above studies focused on the effects of inflow turbulence on gas dispersion in an urban area, but changes in the wind direction were not considered.

Zhang et al. (2011) investigated the effect of real-time flow conditions on the airflow and on the pollutant dispersion in a 2D street canyon, where the horizontal wind speed and wind direction were applied as a single-point measurement at 2 m above a building roof. Significant changes in the wind speed and direction induced the expansion or compression of the primary vortex within the street canyon, resulting in greater pollutant dispersion. They reported that real-time wind boundary conditions yielded better conditions for pollutant dispersion than did steady boundary velocity conditions. However, the observations used by Zhang et al. (2011) exhibited rapid perturbations and the wind speed and wind direction changed significantly over 1 h. Okabayashi et al. (1996) reported that the standard deviation of wind-direction fluctuations ≈ 10 degrees is appropriate to estimate 1-h averaged concentrations. Michioka et al. (2013) implemented a microscale LES model coupled to a mesoscale meteorological model for gas dispersion from the roof of a high-rise building in an urban district under a northerly flow. The ground-level gas concentrations obtained by LES were in good agreement with the field observations. In addition, the LES without coupling with the mesoscale meteorological model overpredicted the ground concentration. When the pollutant is emitted from the roof, the pollutant concentration is significantly affected by wind-direction fluctuations. When the pollutant is emitted within an urban street canyon, the effect of slower perturbations at greater scales, such as wind-direction fluctuations, on gas dispersion remains unclear.

Recently, low-frequency lateral flows were observed within a street canyon. Michioka et al. (2011) used LES for 3D street canyons with aspect ratios of one and two, and reported that lateral flows from one side of a block typically dominated the entire span of the canyon and reached the far side of the block. Inagaki et al. (2012) reported that the locations and directions of significantly large coherent structures of fluctuations in the spanwise velocity component within the canopy are related to the locations of low-momentum fluid above the canopy. Michioka et al. (2018) investigated the lateral flow within the canopy using LES, and found that the low-frequency turbulent flow within the canopy was generated close to the bottom surface around the first row and developed as the fetch increased. However, they were unable to determine the reason for the lateral instantaneous flow passing through the canyon at a lower frequency. To address the mechanism, it is essential to determine whether there is low-frequency flow within the canopy when considering wind-direction fluctuations.

In the present study, large-eddy simulations are implemented for gas dispersion in a cubical canopy with and without wind-direction fluctuations, to address the following questions,

(1) How do wind-direction fluctuations affect gas dispersion emitted from a ground-level line source?
(2) Is low-frequency flow within the canopy observed when considering wind-direction fluctuations?

The organization of the paper is as follows. The computational conditions and numerical set-up are discussed in Sect. 2, and using the LES results, we then discuss the gas dispersion and the low-frequency flow within the canopy in Sect. 3. The canopy is defined as the space below the top of a cubic block, and a canyon is defined as the space between an upwind block and a downwind block.

2 Computational Set-Up

Figure 1 shows a schematic diagram of the computational domain with dimensions of 8.725 m × 0.75 m × 1.0 m for the $x \times y \times z$ grid, respectively. The streamwise, spanwise, and vertical directions are the x-, y-, and z-axes, respectively, and the origin of the coordinate
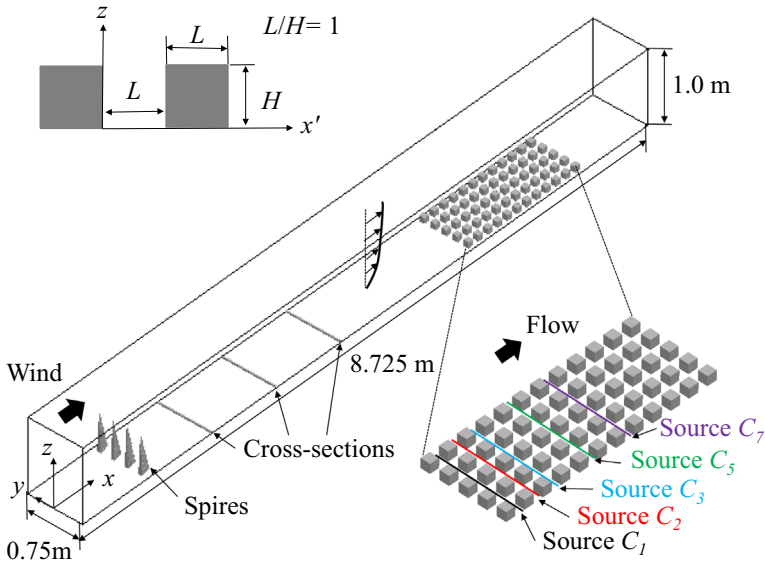
Fig. 1 Computational domain and block layout

axis is the centre of the bottom surface at the entrance of the computational domain. Square blocks with side lengths H of 0.075 m are assumed as a 1/300-scale model, with the square blocks arranged regularly on the bottom surface at equal intervals of H. The front face of the first block is located at $x = 6.0$ m, and the block array comprises 12 rows aligned in the streamwise direction. To generate the approaching turbulent flow, triangular pyramids and cross sections are used, with four triangular pyramids of height 0.6 m set on the bottom surface at $x = 1.0$ m with equal intervals in the spanwise direction. Three cross-sections with 0.75 m in length and 0.02 m in height and width are located on the bottom surface at $x = 2.0$, 3.0, and 4.0 m. The computational mesh system (which include the spires) comprises an orthogonal grid; the sizes of the computational domain, the positions of the triangular pyramids and the cross sections are based on those with the LES model used by Michioka et al. (2016, 2018). A uniform grid spacing with $dx = dy = dz = H/40$, which is sufficient to obtain the second-order velocity and concentration statistics, is used in the spaces between the blocks (Coceal et al. 2006, 2007, Letzel et al. 2008, Branford et al. 2011). The grid is geometrically stretched away from the canopy toward the top boundary, and the cell expansion ratio, that is the ratio of the final grid width to the first grid width, is 15. The number of LES grid points is approximately 5.9×10^7, and the computational domain and grid are the same as those in Michioka et al. (2018).

The filtered continuity, momentum, and mass conservation equations are as follows,

$$\frac{\partial \overline{U_i}}{\partial x_i} = 0, \tag{1}$$

$$\frac{\partial \overline{U_i}}{\partial t} + \frac{\partial \overline{U_j}\,\overline{U_i}}{\partial x_j} = -\frac{1}{\rho}\frac{\partial \overline{P}}{\partial x_i} + \frac{\partial}{\partial x_j}\left\{ (\nu + \nu_t)\left(\frac{\partial \overline{U_i}}{\partial x_j} + \frac{\partial \overline{U_j}}{\partial x_i} \right) \right\}, \tag{2}$$

$$\frac{\partial \overline{C_i}}{\partial t} + \frac{\partial \overline{U}_j \overline{C_i}}{\partial x_j} = \frac{\partial}{\partial x_j} \left\{ \left(D + \frac{\nu_t}{Sc_t} \right) \frac{\partial \overline{C_i}}{\partial x_j} \right\} + S_{i,q}, \tag{3}$$

where an overbar denotes a filtered value, U_i is a velocity component, C_i is the concentration of tracer gas i, P is the pressure, ρ is the density, ν is the kinetic viscosity ($= 1.5 \times 10^{-5}$ m^2 s^{-1}) of air, D ($= 1.5 \times 10^{-5}$ m^2 s^{-1}) is the molecular diffusion coefficient of gas in the air, and $S_{i,q}$ is the source term of the tracer gas i. The subgrid turbulent Schmidt number Sc_t is set to 0.5 (Antonopoulos-Domis 1981), and the subgrid eddy viscosity ν_t is modelled using the standard Smagorinsky model with a Smagorinsky constant of 0.1 (Deardorff 1970). The governing equations are solved directly using the PIMPLEsolver in an open-source code package (OpenFOAM 2.1.1) that uses a finite-volume method. This solver was also used in the LES studies conducted by Michioka and Sato (2012), Michioka et al. (2017, 2018) and Michioka (2018).

No-slip boundary conditions are applied to the bottom surface and the block surfaces and slip boundary conditions are imposed on the velocity components at the upper boundary. Under slip boundary conditions, the velocity normal to the free-slip wall is zero. To eliminate the effects of the side wall, periodic boundary conditions are imposed on velocity components in the spanwise direction.

Four simulations were performed. In these simulations, the inflow velocity components were given as

$$\bar{U}(\theta) = U_{int} \cos\theta = U_{int} \cos\omega t, \tag{4a}$$

$$\bar{V}(\theta) = U_{int} \sin\theta = U_{int} \sin\omega t, \tag{4b}$$

$$\bar{W}(\theta) = 0, \tag{4c}$$

where U_{int} ($= 3.0$ m s^{-1}) is the scalar velocity at the inlet boundary, ω is the angular speed of the wind direction, and θ is the wind direction defined as the counter-clockwise angle from the negative x-axis. Turbulent fluctuations were not provided at the inlet boundary. Figure 2 shows the time history of the wind direction at the inlet boundary ($x = 0$). In case 1, the value of θ is set as zero since wind-direction fluctuations were not considered, and in case 2, a regular pattern of wind-direction fluctuations is assumed. The standard deviation of the wind direction σ_θ is set as 10 degrees, corresponding to the value of σ_θ over 1 h (Okabayashi et al. 1996). To constrain the probability density distribution F of the wind direction as a Gaussian distribution, the angular speed ω is given as,

$$\omega(\theta) = \frac{K}{F(\theta)T}, \tag{5}$$

where T is the period of the wind-direction fluctuation, and K is a constant (Okabayashi et al. 1991). The value of K is adjusted to match the period of the wind-direction fluctuation generated by Eq. 5 and the given value of T. Regular wind-direction fluctuations were repeated every 10 s ($T = 10$ s) as shown in Fig. 2. The period of 10 s is much larger than the integral time scale of turbulence in the seventh row both within the canopy ($z/H = 0.5$) of 0.27 s and above the canopy ($z/H = 1.5$) of 0.12 s in case 1. The length scale and velocity scale ratios between the wind tunnel and the atmosphere are assumed to be 1:300 and 1:1, respectively. The time scale in the LES model (t^m) is converted to the time scale (t^a) in the real atmosphere using

$$t^a = t^m \left(\frac{L^m}{L^a} \right) \left(\frac{U^a}{U^m} \right), \tag{6}$$

Fig. 2 Time history of wind direction at the inlet boundary ($x = 0$)
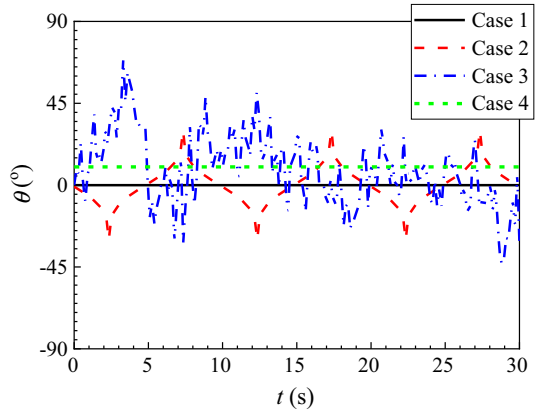
where t and L represent time and length scales, and the superscripts a and m indicate the atmosphere and wind tunnel, respectively. The 10-s interval corresponds to approximately 33 min in the real atmosphere. In case 3, the time history of the observed wind direction is used, as measured 5 m above the roof of the building (approximately 13 m above ground-level) at Komae-shi, Tokyo in Japan by Michioka et al. (2013). The time period corresponds to 1330–1630 local time on February 3, 2005. The actual time of the observation is converted to the time used in the LES model using Eq. 6. In case 4, the wind direction is set at a constant 10 degrees to investigate the flow and concentration pattern within the canopy for an oblique flow.

As can be seen in Fig. 1, five tracer gases with concentrations Ci (C_1, C_2, C_3, C_5, and C_7) were released simultaneously from ground-level continuous-pollutant line sources placed parallel to the spanwise axis at transverse streets to represent vehicular emissions. The index i denotes the location from which the tracer gases were released and indicates that the line sources were placed within the first, second, third, fifth, and seventh rows, respectively. The tracer gases were released at a steady emission rate Q from a continuous ground-level line source located at the first grid points from the bottom surface parallel to the spanwise axis at the central row. In the wind-tunnel experiments of Meroney et al. (1996) and Pavageau and Schatzmann (1999), a line source was made from pipes consisting of regularly spaced holes and the source was covered with a thin metal strip canopy. Since the exhaust of the tracer gas from the line source did not strongly affect the turbulence within the canopy, the release of the tracer gas i is simulated by adding a source term ($S_{i,q}$) to Eq. 3.

Periodic boundary conditions are imposed on the scalar transfer in the spanwise direction. Neumann boundary conditions (a zero-normal derivative, $\partial \overline{C_i}/\partial x_n = 0$, where x_n represents a vector normal to the boundary) are imposed on the scalar transfer of the upper, lower, outlet, and wall boundaries and the condition $Cl_{x=0} = 0$ is imposed on the upstream boundaries of the domain.

The convection term in the momentum equation is discretized using a second-order central scheme. The convection term in the mass conservation equation is discretized using a total-variation-diminishing scheme as the second-order central scheme produced a negative concentration. All other terms are estimated using a second-order central scheme. A first-order Euler implicit temporal discretization is used for the time derivative term, and a timestep of 2.5×10^{-4} s is used. The algorithm used for the resolution of the governing equations is based on the pressure-implicit with splitting of operations method (Issa 1986).

3 Results

3.1 Velocity Statistics

Figure 3 shows the vertical distributions of the mean streamwise velocity component $\langle \bar{U} \rangle$, the standard deviations of the fluctuations in the streamwise and spanwise velocity components, σ_u and σ_v, respectively, the mean wind angle and the standard deviation of the wind angle σ_α at $x = 5.5$ m and $y = 0$, which was 0.5 m upwind from the front face of the first block array. Here, $\langle \rangle$ denotes the time-averaged values over 50 s. The value of σ_α was estimated from time series data of instantaneous wind angle α using $\sigma_\alpha = \sqrt{(\alpha - \langle \alpha \rangle)^2}$, where $\alpha = \tan^{-1}(\bar{V}/\bar{U})$ is the instantaneous wind angle. The boundary-layer thickness is $z = 7H$, which was defined as the height in which the mean streamwise velocity component is equal to 99% of the freestream wind speed U_{ref}. The power index of the power law for the mean streamwise velocity profiles is approximately 1/6, representing flow over suburban structures and low-rise buildings. The values of σ_u is quite small for $z/H = 5.5$, mainly because the the velocity statistics are estimated using grid-scale velocities without considering the subgrid-scale velocity fluctuations. The Reynolds number based on the freestream at $x = 5.5$ m is approximately 11×10^5. The profile of the mean streamwise velocity components in cases 1–4 is similar, while the values of σ_v in cases 2 and 3 are two to three times greater than those in case 1. These increases are not caused by turbulent fluctuations, but by wind-direction fluctuations, and the value of σ_u in cases 2 and 3 also increases with increasing σ_v. The standard deviation of the wind angle at $z/H = 1.0$ in cases 1 and 4 is approximately 4 degrees, which corresponds to the value of σ_α in the wind-tunnel experiment without wind-direction fluctuations (Okabayashi et al. 1991). The values of σ_α for $z/H < 1.5$ is approximately 10 degrees in case 2 and 12 degrees in case 3, indicating that the turbulent flow including wind-direction fluctuation is generated in the inflow turbulent flow.

Figure 4 shows the power spectra of fluctuations in streamwise and spanwise velocity components E_u and E_v at $x = 5.5$ m and $z = H$, with the frequency f normalized by block height H and the value of $\langle \bar{U} \rangle$ at $z = 2H$, U_0. In all cases, the first or second peak of fE_u and fE_u is observed at $f H/U_0 \approx 1.0 \times 10^{-1}$, corresponding to the larger energy-containing eddies in the boundary layer without wind-direction fluctuation. In case 2 the peak of fE_v is observed for $f H/U_0 \approx 2.0 \times 10^{-3}$, which corresponds to the frequency of the regular wind direction. In case 3, the values of fE_v are enhanced for $f H/U_0 < 3.0 \times 10^{-2}$ by wind-direction fluctuations.

Figure 5 shows the mean velocity distributions for the x–y cross-section around the first row at $z/H = 1.1$; the grey-shaded area indicates the block position and the spanwise velocity component is not normalized. For case 1, the horizontal velocity vector and the spanwise velocity component are approximately symmetrical with the canyon centreline. The flow close to the front face of the first block moves away from the block and then approaches close to the block centre behind the block before tending towards the streamwise direction. By contrast, for the wind direction of $\theta = 10°$ in case 4, it is observed that the faster-moving flow above the streamwise street close to the first block passes over the canyon. The mean flow speed above the space between the blocks for cases 2 and 3 is greater than that in case 1, mainly because the oblique flow, as for case 4, passes over the canyon when the wind direction is tilted, as shown in Fig. 5d.

Figure 6 shows the vertical distributions of the mean streamwise velocity component $\langle \bar{U} \rangle$ and the standard deviations of the fluctuations in the streamwise and spanwise velocity components σ_u, σ_v at the canyon centre ($x' = 0.5H$, $y = 0$) and at the intersection ($x' = 0.5H$,
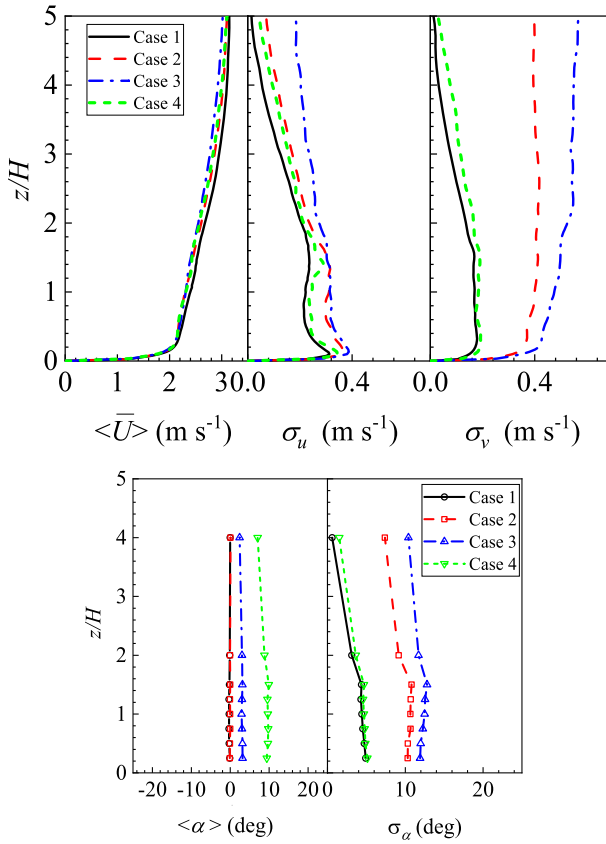
Fig. 3 Vertical distributions of the streamwise velocity component, standard deviations of fluctuations in streamwise and spanwise velocity components, mean wind angle and standard deviations of wind angle at $x = 5.5$ m

$y = H$). Here, $\langle \bar{U} \rangle$, σ_u, and σ_v are normalized by $\langle \bar{U} \rangle$ at $z = 2H$, U_0, and the origin of x' is the bottom of the back face of the front block in each row, as shown in Fig. 1. At the canyon centre in the first row, the mean streamwise velocity component in cases 2–4 is greater than that in case 1 above the canyon. This is attributed to the fact that the faster moving turbulent flow above the streamwise street passes over the canyon because of wind-direction fluctuations. Beyond the third row, the mean streamwise velocity components within the canopy do not vary between the four cases. Therefore, the wind-direction fluctuations marginally affect the mean streamwise velocity component at the first row, and have a negligible effect beyond the third row.

At the canyon centre, the peak values of σ_u in the first row appear above the canyon, and the peak position of $z/H \approx 1.05$ in cases 2–4 is less than that for case 1. In case 1, the flow separation that occurred at the leading edge of the first block primarily affects the peak values of σ_u, but in cases 2–4 the oblique flow also affects the peak values. Above the canopy, wind-direction fluctuations significantly affect the values of σ_v within the canopy the effect of wind-direction fluctuations on the values of σ_v decreases. Within the canopy, the difference in σ_u between the cases becomes negligible beyond the third row, and the values of σ_u approach the wind-tunnel experimental results of Takimoto et al. (2011). However, above the canopy,

Fig. 4 Power spectra of fluctuations in the streamwise and spanwise velocity components E_u and E_v at $x = 5.5$ m, $z = H$
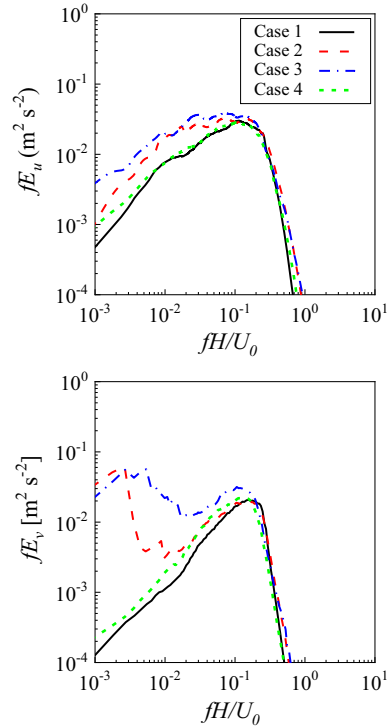
the values of σ_u in case 1 are smaller than the wind-tunnel experimental results for the fully-developed turbulent flow because the values of σ_u in the seventh row still continue to increase as an internal boundary layer develops above the canopy. In addition, above the canopy, the values of σ_u in cases 2 and 3 are marginally greater than the values in case 1. Comparing the values of σ_u between the field observations and the wind-tunnel experiment of Takimoto et al. (2011), the field values increase above the canopy, but the values of σ_u within the canopy are similar. The increase above the canopy is because of the outer-layer fluctuations, which includes wind-direction fluctuations. The values of σ_v in cases 2 and 3 are directly affected by wind-direction fluctuations, but the difference in σ_v within the canopy is negligible beyond the third row. Therefore, the wind-direction fluctuations affect the turbulent intensity above the canopy, but have little effect within the canopy. In addition, close to the bottom surface at the canyon centre, the values of σ_v are typically similar to, or greater than, the values of σ_u, suggesting that a significant lateral flow passes within the canopy. This lateral instantaneous flow is observed irrespective of the wind-direction fluctuations and is discussed later.

Figure 7 shows the vertical distribution of the Reynolds shear stress at the canyon centre ($x' = 0.5H$, $y = 0$) and at the intersection ($x' = 0.5H$, $y = H$). Above the first row at $y = 0$, the position of the Reynolds shear stress in case 1 is different from the position in cases 2–4. This difference corresponds primarily to the peak gradient of the mean streamwise velocity component, as shown in Fig. 6a. In addition, in the third and seventh rows, the Reynolds shear stress above the canyon in cases 2 and 3 is marginally greater than that in case 1. This trend is similar to the comparison of the Reynolds shear stress between the wind-tunnel experiment and field experiments of Takimoto et al. (2011). The comparisons indicated that
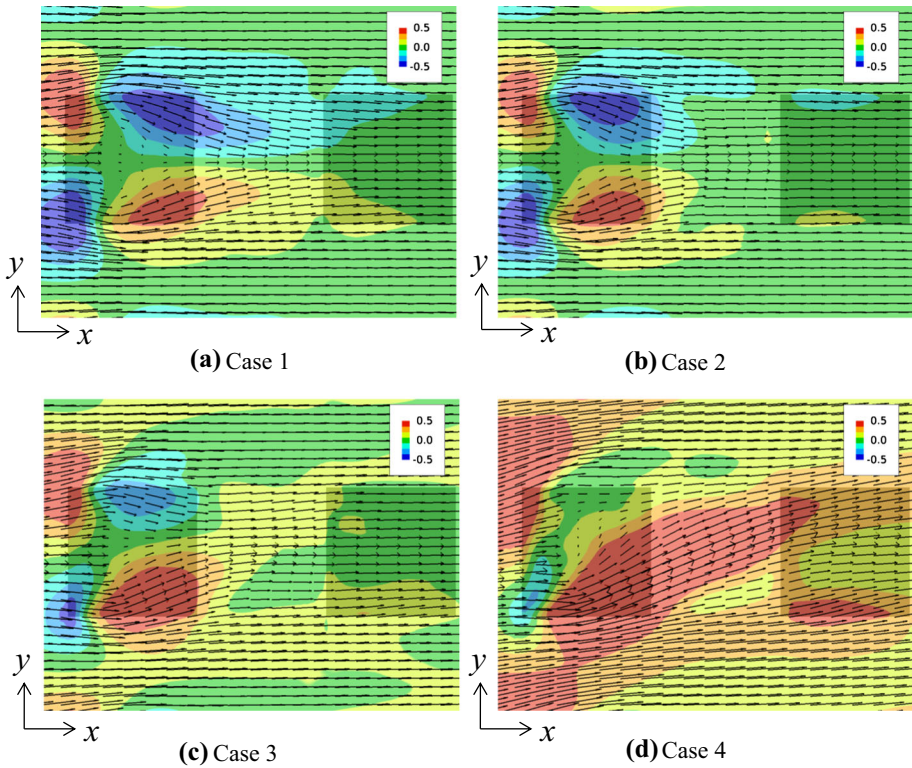
(a) Case 1

(b) Case 2

(c) Case 3

(d) Case 4

Fig. 5 Mean velocity distributions for the x–y cross-section at $z/H = 1.1$. Colour represents the spanwise velocity component (m s^{-1})

the wider peak in the field experiments is considered to be the result of greater wind-direction fluctuations at the observation site.

3.2 Concentration Statistics

Figure 8 shows the vertical distribution of the mean concentrations at $x'/H = 0$, 0.5, and 1.0 at the canyon centre ($y = 0$). The concentration $\overline{C_i}$ is normalized by U_0, block height H, line source length L, and total emissions Q, as follows,

$$\overline{C_i^*} = \frac{\overline{C_i} U_0 H L}{Q}. \tag{7}$$

The mean concentration $\overline{C_i^*}$ at $x'/H = 0$ is significantly greater than the concentration at $x'/H = 1.0$ because the recirculation generated within the canyon transports the pollutant in a leeward direction. As the vertical distribution of the mean concentration is approximately similar in all the rows, wind-direction fluctuations do not significantly affect the gas dispersion at the canyon centre. The mean concentrations in the seventh row correspond to the values of $\left\langle \overline{C_i^*} \right\rangle$ obtained by LES for a fully-developed turbulent flow over a square array of cubical blocks aligned regularly with a plan area density of 0.25 (Michioka et al. 2014). When closely investigated, the mean concentration in the first and third rows in cases 2–4 is
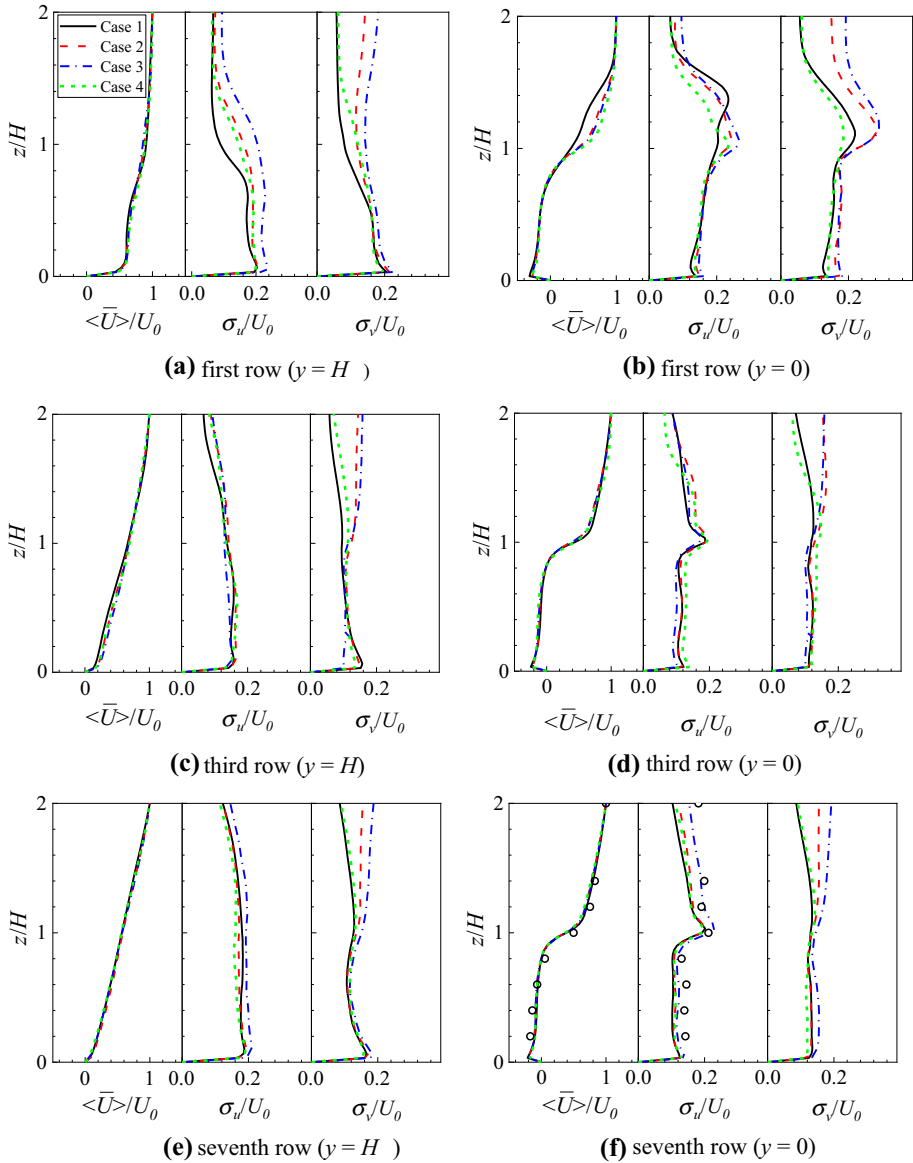
Fig. 6 Vertical distributions of mean streamwise velocity component, standard deviations of fluctuations in streamwise velocity, and spanwise velocity components at canyon centre ($y = 0$), and intersection ($y = H$) at first, third, and seventh rows. Circles represent wind-tunnel experimental results of Takimoto et al. (2011)

marginally greater than the concentration in case 1, and wind-direction fluctuations tend to increase the mean concentration within the canyon at the first and third rows. In order to investigate the marginal increase in the concentration within the canyon caused by wind-direction fluctuations, the spatially-averaged concentration $\left\langle \overline{C_i^*} \right\rangle_{Canyon}$ within the target canyon where the pollutant is emitted is shown in Fig. 9, and defined as follows
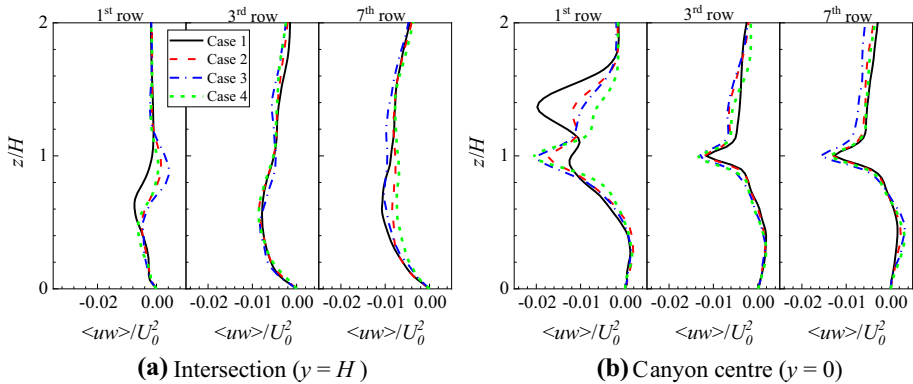
Fig. 7 Vertical distributions of Reynolds shear stress at the first, third, and seventh rows at $x'/H = 0.5$ and $y = 0$

$$\left\langle \overline{C_i^*} \right\rangle_{Canyon} = \frac{1}{V_{canyon}} \int_0^H \int_{-0.5H}^{0.5H} \int_0^H \left\langle \overline{C_i^*} \right\rangle \mathrm{d}x' \mathrm{d}y \mathrm{d}z, \tag{8}$$

where V_{canyon} $(= H^3)$ is the volume of the target canyon. The values of $\left\langle \overline{C_i^*} \right\rangle_{Canyon}$ for case 1 gradually increases until the fifth row when it is approximately three times as great as its value in the first row. Cases 2–4 exhibit similar trends. The values in cases 2 and 3 before the third row are marginally greater than the values in case 1, and the values in cases 2 and 3 are very close beyond the fifth row. Therefore, it can be concluded that wind-direction fluctuations tend to increase the concentration within the canyon before the third row. For the oblique flow in case 4, the value before the third row is marginally greater than the value in case 1. However, beyond the fifth row the value is the least of all the cases. Branford et al. (2011) reported that gas is efficiently transported in the vertical direction and mixes through the canopy depth under a wind direction of zero degrees, whereas for oblique flow the gas disperses widely horizontally and the concentration decays more rapidly with height by topological dispersion such as dividing streamlines because of flow impinging on the blocks (Belcher et al. 2003). In case 4, the topological dispersion decreases the concentration in the seventh row, but the reasons why the concentration increases before the third row in cases 2–4 remain unclear.

The mean velocity vector and mean concentration for the x–y cross-section at $z/H = 0.25$ are shown in Fig. 10. For cases 1–3, the mean lateral flows from the sides of the blocks converge at the canyon centre, and two recirculation flows are generated. In the first row, the recirculation flow in cases 2 and 3 is greater than that for case 1. As the fetch increases, the shape of the recirculation flow in cases 1–3 becomes similar and the difference in the horizontal distribution of the concentration in the seventh row becomes smaller. In case 4, anticlockwise recirculation flow is observed in the seventh row, and at the lower left within the canyon the mean concentration is trapped by the recirculation flow and a significant concentration is observed. However, the horizontal flow close to the front wall of the downwind block transports the gas out of the canyon. Kim and Baik (2004) used a RANS-based simulation for gas dispersion in an idealized street canyon under a wind direction of 15 degrees, and reported one anticlockwise recirculation flow within the canyon at $z/H = 0.5$. Although the height and wind directions were marginally different from the RANS approach

Fig. 8 Vertical distributions of mean concentration at $x'/H = 0$, 0.5, and 1.0 and $y = 0$ at the first, third, and seventh rows

(a) first row

(b) third row
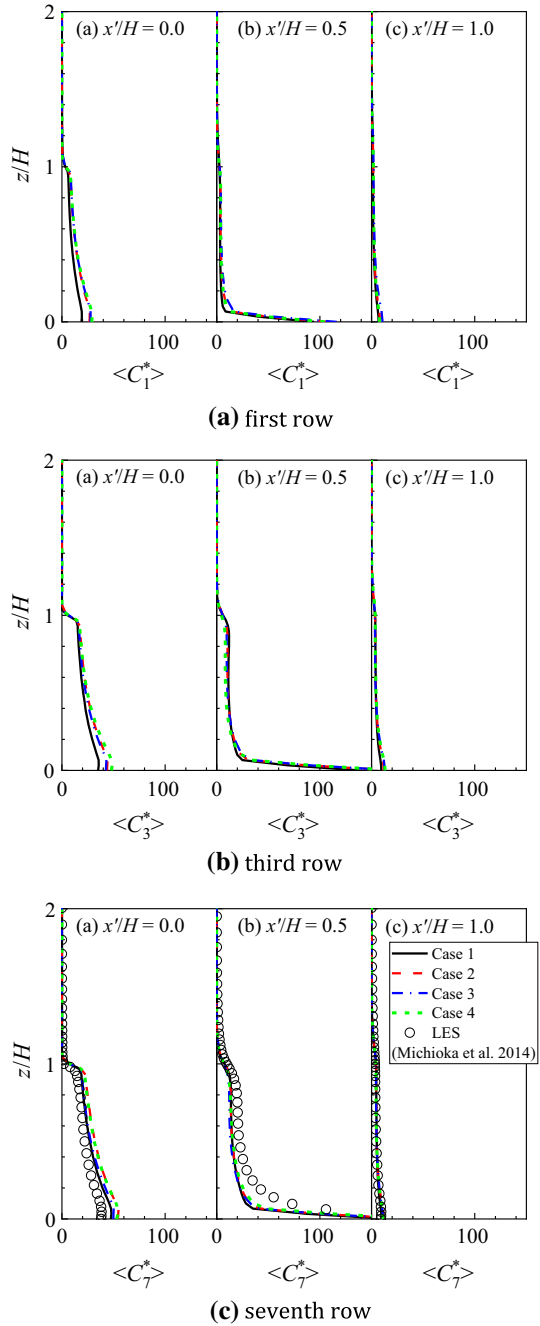
(c) seventh row

of Kim and Baik (2004), approximately the same flow pattern is observed in the seventh row (Fig. 10d). However, it is noteworthy that the shape of the recirculation flow in case 4 changes significantly with fetch. In the third row, two recirculating flows are observed for

Fig. 9 Spatially-averaged concentration within the target canyon
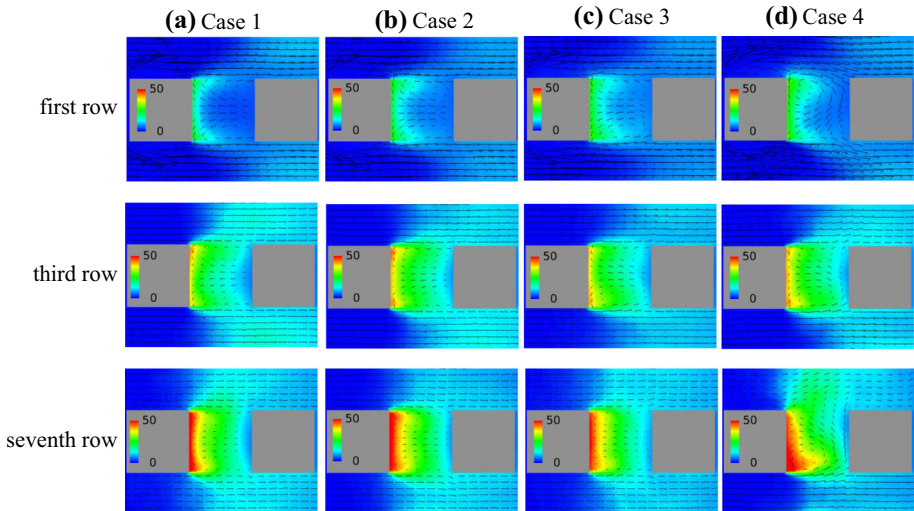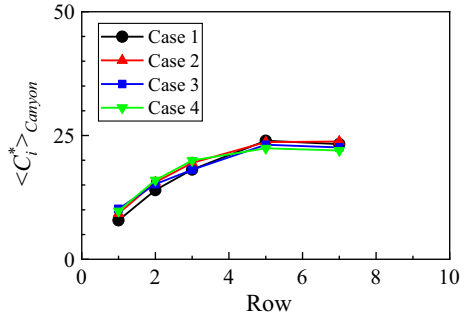
Fig. 10 Mean velocity vector and mean concentration for the x–y cross-section at $z/H = 0.25$. Colour represents the normalized mean concentration

cases 1–3, but in the first row a clockwise recirculation flow is observed that is significantly different from the flow in the third and seventh rows. In case 4, the flow separates at the upper left and lower left edges of the first block. As the upper separation zone is greater than the lower one, the flow separating from the upper left edge runs into the canyon and a clockwise recirculation flow is generated. As the fetch increases, the lateral flow from the lower street gradually dominates and anticlockwise recirculation is generated within the canyon as the wind direction above the canopy is 10 degrees.

Snapshots of the instantaneous velocity vector and concentration for the x–y cross-section around the first row at $z/H = 0.25$ for case 2 are shown in Fig. 11. When the wind direction is approximately 10 degrees, as shown in Fig. 11a, the flow largely separates at the upper left edge of the first block and runs into the canyon. The instantaneous clockwise recirculation flow is observed within the canyon, and the flow is trapped within the canyon. As was frequently noted in case 4, the clockwise recirculation flow is observed within the first canyon, as shown in Fig. 10d. When the wind direction is primarily perpendicular to the front face of the block, the lateral flow from the sides of the blocks at times dominates the entire span of the canyon, as shown in Fig. 11b. When the wind direction is approximately
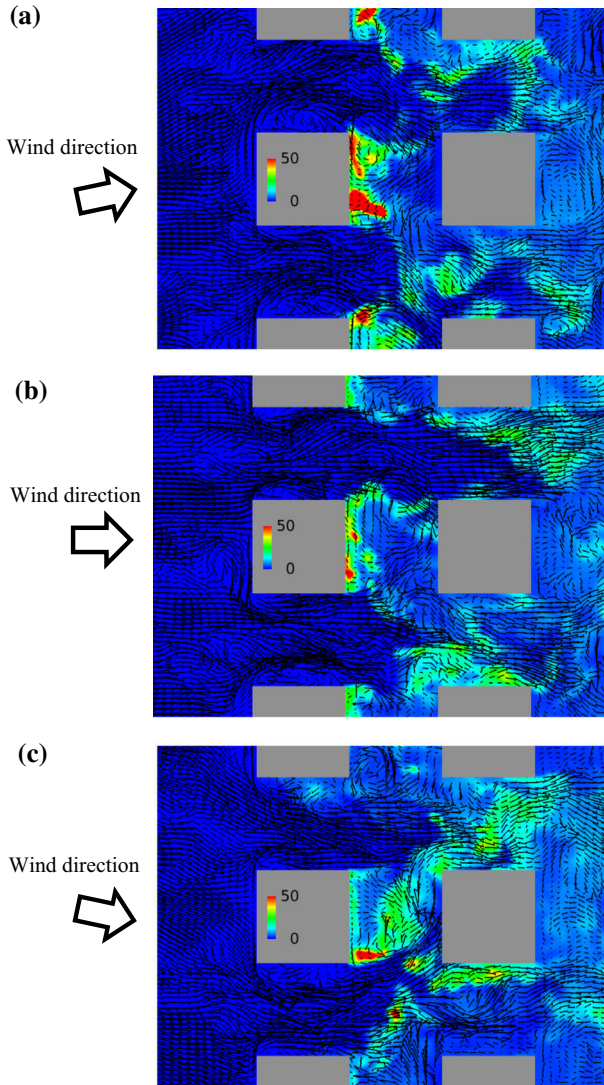
(a)

Wind direction

(b)

Wind direction

(c)

Wind direction

Fig. 11 Snapshots of instantaneous velocity vector and concentration for the x–y cross-section at $z/H = 0.25$ in case 2. Colour represents the instantaneous concentration

−10 degrees, as shown in Fig. 11c, the flow primarily separates at the lower left edge of the first block, and instantaneous anticlockwise recirculation is observed within the canyon. Therefore, when the wind direction is changed, greater recirculation is generated within the canyon, and this tends to increase the concentration within the canyon.

Figure 12 shows the streamwise distributions of the mean concentration at $y = H$ emitted from sources C_1, C_3, and C_7; here, x_{C1}, x_{C3}, and x_{C7} represent the streamwise position of sources C_1, C_3, and C_7, respectively. As wind-direction fluctuations increase the concentration within the canyon before the third row as shown in Fig. 9, the mean concentration in the streamwise street pathway tends to decrease with wind-direction fluctuations for sources
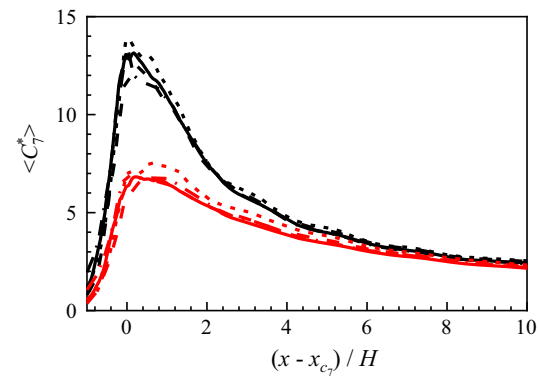
Fig. 12 Streamwise distributions of mean concentration at $z/H = 0.25$ and $z/H = 0.75$
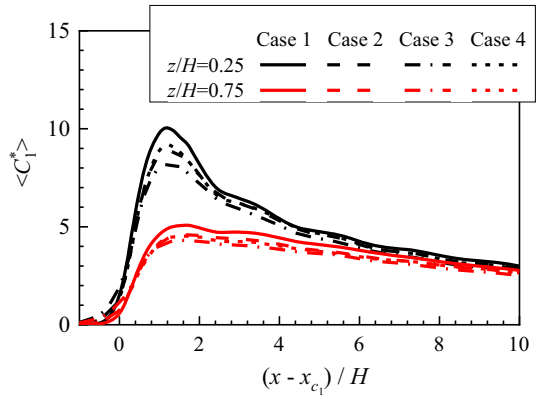

(a) Source C_1
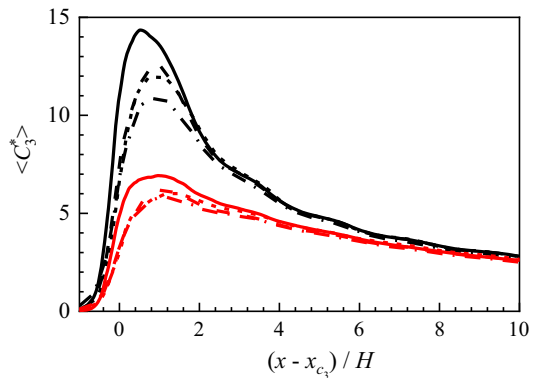

(b) Source C_3

(c) Source C_7

C_1 and C_3. However, the concentration difference across all cases decreases with increasing fetch. Wind-direction fluctuations only marginally affect gas dispersion close to sources before the third row. For source C_7, the concentration distributions for cases 1–3 are similar as the wind-direction fluctuations do not significantly affect the mean velocity and the turbu-
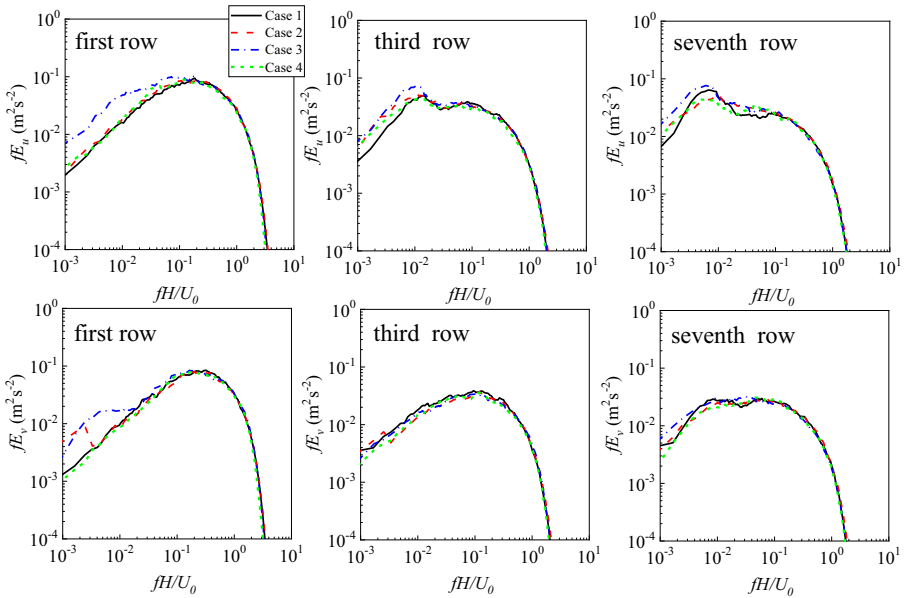
(a) Intersection ($y = H$) at $z/H = 0.25$
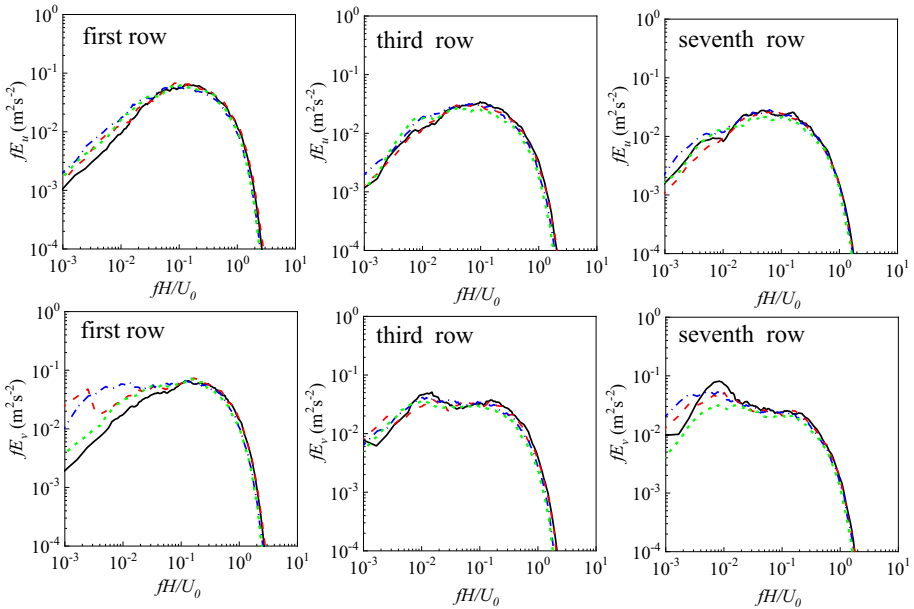
(b) Canyon ($y = 0$) at $z/H = 0.25$

Fig. 13 Power spectra of fluctuations in the streamwise and spanwise velocity components E_u and E_v at $x'/H = 0.75$ at $z/H = 0.25$

lence intensity in the seventh row, as shown in Fig. 6e, f. Note that the mean concentration in case 4 is marginally greater than that in the other cases as the oblique flow transports the gas out of the canyon.

3.3 Low-Frequency Turbulence

Figure 13 shows the power spectra of the fluctuations in the streamwise and spanwise velocity components E_u and E_v at $x'/H = 0.75$ at both the intersection and canyon centre, where significant standard deviations of the fluctuation in the spanwise velocity component were observed close to the surface without wind-direction fluctuations (Michioka et al. 2018).

First, in the first row at both the canyon centre and the intersection, the value of fE_v for $fH/U_0 < 4.0 \times 10^{-3}$ for cases 2 and 3 is greater than the values for cases 1 and 4, which indicates that the turbulent flow induced by wind-direction fluctuations affects the turbulent flow close to the bottom surface. In addition, a second peak of fE_v is observed at $fH/U_0 \approx 2.0 \times 10^{-3}$ for case 2, and corresponds to the frequency of the imposed periodic wind direcion. The value of fE_u at the canyon centre for $fH/U_0 < 0.1$ for case 3 is greater than the value for case 1, implying a significant increase in streamwise turbulent motion in the first row. This is related to the significant value of σ_u at the approaching flow at $x = 5.5$ m because of wind-direction fluctuations.

Second, in the third row, the values of fE_v for cases 2 and 3 for $fH/U_0 < 4.0 \times 10^{-3}$ become smaller than those in the first row, and for $fH/U_0 \approx 8.0 \times 10^{-3}$ the values of fE_u for all cases at the intersection and the values of fE_v at the canyon centre increase. In the approaching turbulent flow as shown in Fig. 4, except for case 3 the apparent peaks at $fH/U_0 \approx 8.0 \times 10^{-3}$ are not observed for fE_u and fE_v. This suggests that these peaks are less sensitive to the approaching flow, but further study is required to understand the effect of the inflow characteristics on the low-frequency turbulent motion. Michioka et al. (2018) reported that, without wind-direction fluctuations, the low-frequency turbulent flow developed as the fetch increased, and the lateral instantaneous turbulent flows ultimately passed through the canyon at a low frequency. With wind-direction fluctuations and oblique flow the low-frequency turbulent flow is observed at the third row.

Third, in the seventh row at the canyon centre, the value of fE_v at the canyon centre and the value of fE_u at the intersection for cases 2 and 3 for $fH/U_0 < 8.0 \times 10^{-3}$ become larger than those in case 1. This indicates that low-frequency turbulent flow with near-constant intervals is not generated, but the low-frequency turbulent flow with frequencies $fH/U_0 < 8.0 \times 10^{-3}$ is generated within the canopy under wind-direction fluctuations. For case 4, the values of fE_v for $fH/U_0 < 8.0 \times 10^{-3}$ are smaller than for cases 1–3, but the value of fE_u for $fH/U_0 < 8.0 \times 10^{-3}$ is relatively large. This indicates that low-frequency turbulent flow from both sides of the canyon alternately passing through the canyon at near-constant interval is not generated. This is because the lateral instantaneous flow from the upper street seldom passes the canyon, and the instantaneous lateral flow from the lower street is typically dominant within the canyon as shown in Fig. 10d. Therefore, under oblique flow, the low-frequency turbulent flow is also generated within the canopy.

4 Summary and Conclusions

Large-eddy simulations of gas dispersion in an idealized street canyon has been used to investigate the effect of wind-direction fluctuations on gas dispersion within the canopy. Square blocks were placed on the bottom surface at equal intervals, and line sources were placed within the first, second, third, fifth and seventh rows.

The wind-direction fluctuations marginally affected the mean streamwise velocity component in the first row above the canopy, but these were not significantly affected beyond

the third row. The standards deviation of the fluctuations in the streamwise and spanwise velocity components above the canopy were also affected by wind-direction fluctuations, but the values within the canopy were less sensitive to the fluctuations beyond the third row. The wind-direction fluctuations affected the turbulence intensities above the canopy, but did not significantly affect them within the canopy.

The spatially-averaged concentrations with wind-direction fluctuations before the third row were marginally greater than the values without fluctuations, and is related to the size of the recirculation flow in the $x–y$ cross-section in the first row. The wind-direction fluctuations increased the size of the recirculation flow within the canopy, and the greater recirculation flow trapped the gas within the canyon. Therefore, wind-direction fluctuations tended to increase the concentration within the canyon before the third row. Beyond the fifth row, the concentrations both with and without wind-direction fluctuations were essentially similar.

The lateral instantaneous turbulent flow with a low-frequency pass through the canyon was generated both with and without wind-direction fluctuations. However, how the wind-direction fluctuations affect the low-frequency flow and instantaneous lateral flow is still unclear. Further work is needed to comprehend the effect of wind-direction fluctuations on the instantaneous turbulent flow within the canopy.

References

An K, Fung JCH, Yim SHL (2013) Sensitivity of inflow boundary conditions on downstream wind and turbulence profiles through building obstacles using a CFD approach. J Wind Eng Ind Aerodyn 115:137–149

Antonopoulos-Domis M (1981) Large eddy simulation of a passive scalar in isotropic turbulence. J Fluid Mech 104:55–79

Arnold SJ, Apsimon H, Barlow J, Belcher S, Bell M, Boddy JW, Britter R, Cheng H, Clark R, Colvile RN, Dimitroulopoulouh S, Dobre A, Greally B, Kaur S, Knights A, Lawton T, Makepeace A, Martin D, Neophytou M, Neville S, Nieuwenhuijsen M, Nickless G, Price C, Robin A, Shallcross D, Simmonds P, Smalley RJ, Tate J, Tomlin AS, Wang H, Walsh P (2004) Introduction to the DAPPLE air pollution project. Sci Total Environ 332:139–153

Belcher SE, Jerram N, Hunt JCR (2003) Adjustment of a turbulent boundary layer to a canopy of roughness elements. J Fluid Mech 488:369–398

Branford S, Coceal O, Thomas TG, Belcher SE (2011) Dispersion of a point-source release of a passive scalar through an urban-like array for different wind. Boundary-Layer Meteorol 139:367–394

Cai X-M, Barlow JF, Belcher SE (2008) Dispersion and transfer of passive scalars in and above street canyons—Large-eddy simulations. Atmos Environ 42:5885–5895

Cheng WC, Liu C-H (2011) Large-eddy simulation of flow and pollutant transports in and above two-dimensional idealized street canyon. Boundary-Layer Meteorol 139:411–437

Coceal O, Thomas TG, Castro IP, Belcher SE (2006) Mean flow and turbulence statistics over groups of urban-like cubical obstacles. Boundary-Layer Meteorol 121:491–519

Coceal O, Thomas TG, Belcher SE (2007) Spatial variability of flow statistics within regular building arrays. Boundary-Layer Meteorol 125:537–552

Deardorff JW (1970) A numerical study of three-dimensional turbulent channel flow at large Reynolds numbers. J Fluid Mech 41:453–480

Duan G, Ngan K (2018) Effects of time-dependent inflow perturbations on turbulent flow in a street canyon. Boundary-Layer Meteorol 167:257–284

Inagaki A, Castillo MCL, Yamashita Y, Kanda M, Takimoto H (2012) Large-eddy simulation of coherent flow structures within a cubical canopy. Boundary-Layer Meteorol 142:207–222

Issa R (1986) Solution of implicitly discretized fluid flow equations by operator splitting. J Comput Phys 62:40–65

Kim J-J, Baik J-J (2004) A numerical study of the effects of ambient wind direction on flow and dispersion in urban street canyons using the RNG k-ε turbulence model. Atmos Environ 38:3039–3048

Letzel M, Krane M, Raasch S (2008) High resolution urban large-eddy simulation studies from street canyon to neighborhood scale. Atmos Environ 42:8770–8784

Meroney R, Pavageau M, Rafailidis S, Schatzmann M (1996) Study of line source characteristics for 2-D physical modeling of pollutant dispersion in street canyons. J Wind Eng Ind Aerodyn 62:37–56

Michioka T (2018) Large-eddy simulation for turbulent flow and gas dispersion over wavy walls. Int J Heat Mass Transf 125:569–579

Michioka T, Sato A (2012) Effect of incoming turbulent structure on pollutant removal from two-dimensional street canyon. Boundary-Layer Meteorol 145:469–484

Michioka T, Sato A, Takimoto H, Kanda M (2011) Large-eddy simulation for the mechanism of pollutant removal from a two-dimensional street canyon. Boundary-Layer Meteorol 138:195–213

Michioka T, Sato A, Sada K (2013) Large-eddy simulation coupled to mesoscale meteorological model for gas dispersion in an urban district. Atmos Environ 75:153–162

Michioka T, Takimoto H, Sato A (2014) Large-eddy simulation of pollutant removal from a three-dimensional street canyon. Boundary-Layer Meteorol 150:259–275

Michioka T, Takimoto H, Ono H, Sato A (2016) Effect of fetch on a mechanism for pollutant removal from a two-dimensional street canyon. Boundary-Layer Meteorol 160:185–199

Michioka T, Takimoto H, Ono H, Sato A (2017) Reynolds-number dependence of gas dispersion over a wavy wall. Boundary-Layer Meteorol 164:401–418

Michioka T, Takimoto H, Ono H, Sato A (2018) Effects of fetch on turbulent flow and pollutant dispersion within a cubical canopy. Boundary-Layer Meteorol 168:247–267

Murena F, Mele B (2014) Effect of short-time variations of wind velocity on mass transfer between street canyons and the atmospheric boundary layer. Atoms Pollt Res 5:484–490

Nozu T, Tamura T (2012) LES of turbulent wind and gas dispersion in a city. J Wind Eng Ind Aerodyn 104–106:492–499

Okabayashi K, Ide Y, Takahashi H, Kane N, Okamoto S, Kobayashi K (1991) A new wind tunnel technique for investigating gas diffusion behind a structure. Atmos Environ 25A:1227–1236

Okabayashi K, Ide Y, Kitabayashi K, Okamoto S, Kobayashi K (1996) Effect of wind directional fluctuations on gas diffusion over a model terrain. Atmos Environ 30:2871–2880

Pavageau M, Schatzmann M (1999) Wind tunnel measurements of concentration fluctuations in an urban street canyon. Atmos Environ 33:3961–3971

Takimoto H, Sato A, Barlow JF, Moriwaki R, Inagaki A, Onomura S, Kanda M (2011) Particle image velocimetry measurements of turbulent flow within outdoor and indoor urban scale models and flushing motions in urban canopy layers. Boundary-Layer Meteorol 140:295–314

Tominaga Y, Stathopoulos T (2011) CFD modeling of pollution dispersion in a street canyon: Comparison between LES and RANS. J Wind Eng Ind Aerodyn 99:340–348

Xie ZT (2011) Modelling street-scale flow and dispersion in realistic winds—towards coupling with mesoscale meteorological models. Boundary-Layer Meteorol 141:53–75

Xie ZT, Castro IP (2009) Large-eddy simulation for flow and dispersion in urban streets. Atmos Environ 43:2174–2185

Zhang YW, Gu ZL, Cheng Y, Lee SC (2011) Effect of real-time boundary wind conditions on the air flow and pollutant dispersion in an urban street canyon-Large eddy simulations. Atmos Environ 45:3352–3359